remote sensing

MDPI

Article

Variation of Aerosol Optical Depth Measured by Sun Photometer at a Rural Site near Beijing during the 2017–2019 Period

Xiu Wu [1], Jinlong Yuan [1,2], Tianwen Wei [1], Yunpeng Zhang [1], Kenan Wu [1] and Haiyun Xia [1,2,3,4,*]

[1] School of Earth and Space Science, University of Science and Technology of China, Hefei 230026, China; wuxiu@mail.ustc.edu.cn (X.W.); yuanjinl@mail.ustc.edu.cn (J.Y.); twwei@mail.ustc.edu.cn (T.W.); zyp110@mail.ustc.edu.cn (Y.Z.); wkn924@mail.ustc.edu.cn (K.W.)
[2] School of Atmospheric Physics, Nanjing University of Information Science and Technology, Nanjing 210044, China
[3] National Laboratory for Physical Sciences at the Microscale, University of Science and Technology of China, Hefei 230026, China
[4] Institute of Software, Chinese Academy of Sciences, Beijing 100190, China
* Correspondence: hsia@ustc.edu.cn

Abstract: In recent years, the Beijing–Tianjin–Hebei region has become one of the worst areas for haze pollution in China. Sun photometers are widely used for aerosol optical property monitoring due to the advantages of fully automatic acquisition, simple maintenance, standardization of data processing, and low uncertainty. Research sites are mostly concentrated in cities, while the long-term analysis of aerosol optical depth (AOD) for the pollution transmission channel in rural Beijing is still lacking. Here, we obtained an AOD monitoring dataset from August 2017 to March 2019 using the ground-based CE-318 sun photometer at the Gucheng meteorological observation site in southwest Beijing. These sun photometer AOD data were used for the ground-based validation of MODIS (Moderate Resolution Imaging Spectroradiometer) and AHI (Advanced Himawari Imager) AOD data. It was found that MODIS and AHI can reflect AOD variation trends by sun photometer on daily, monthly, and seasonal scales. The original AOD measurements of the sun photometer show good correlations with satellite observations by MODIS (R = 0.97), and AHI (R = 0.89), respectively, corresponding to their different optimal spatial and temporal windows for matching with collocated satellite ground pixels. However, MODIS is less stable for aerosols of different concentrations and particle sizes. Most of the linear regression intercepts between the satellite and the photometer are less than 0.1, indicating that the errors due to surface reflectance in the inversion are small, and the slope is least biased (AHI: slope = 0.91, MODIS: slope = 0.18) in the noon period (11 a.m.–2 p.m.) and most biased in summer (AHI: slope = 0.77, MODIS: slope = 1.31), probably due to errors in the aerosol model. The daily and seasonal variation trends between CE-318 AOD measurements in the Gucheng site and fine particulate observations from the national air quality site nearby were also compared and investigated. In addition, a typical haze–dust complex pollution event in North China was analyzed and the changes in AOD during the pollution event were quantified. In processing, we use sun photometer and satellite AOD data in combination with meteorological and PM data. Overall, this paper has implications for the study of AOD evolution patterns at different time scales, the association between $PM_{2.5}$ concentrations and AOD changes, and pollution monitoring.

Keywords: aerosol; remote sensing; air pollution; ground-based validation; $PM_{2.5}$

Citation: Wu, X.; Yuan, J.; Wei, T.; Zhang, Y.; Wu, K.; Xia, H. Variation of Aerosol Optical Depth Measured by Sun Photometer at a Rural Site near Beijing during the 2017–2019 Period. *Remote Sens.* **2022**, *14*, 2908. https://doi.org/10.3390/rs14122908

Academic Editors: Ka Lok Chan, Youwen Sun and Feng Zhang

Received: 29 April 2022
Accepted: 15 June 2022
Published: 17 June 2022

1. Introduction

In recent decades, with industrialization and a dramatic rise in population, the problem of atmospheric pollution has become increasingly serious [1]. The culprits of atmospheric pollution are particulate pollutants and gaseous pollutants in the atmosphere [2]. As major particulate pollutants, aerosols generally have particle diameters between 0.01 and 10 microns [3]. The sources of atmospheric aerosol pollution are primary and secondary emissions [4].

Primary aerosols are products directly emitted into the atmosphere from pollution sources without physicochemical reactions (mainly pollen, soot, sea salt particles, etc.). Secondary aerosols comprise new particulate matter generated from various gaseous (SO_2, NO_x) or particulate pollutants (volatile organic compounds) already present in the atmosphere after oxidation reactions with ozone, hydroxyl radicals, etc., under the irradiation of ultraviolet light [5,6].

Aerosols can affect global climate change through radiative forcing [7] and by influencing cloud microphysics processes [8], while also contributing to the processes involved with haze [9,10] and acid rain formation [11]. In addition, high $PM_{2.5}$ concentrations can contribute to the development of various respiratory diseases [12] and oxidative damage to human DNA [13]. With a coal-dominated energy structure and high energy consumption [14] in the Beijing–Tianjin–Hebei region of China, a unique topography that is not conducive to pollutant dispersion [15], and transmission from heavily polluted surrounding regions [16,17], particulate matter concentrations have far exceeded their environmental capacity by several times [18]. For these reasons, China's State Council issued the Action Plan for the Prevention and Control of Air Pollution in September 2013, and after the policy was implemented, $PM_{2.5}$ concentrations in the Beijing–Tianjin–Hebei region dropped by 39.1% and PM_{10} decreased by more than 20% between 2013 and 2017 [19]. With the continuous increase in social requirements for environmental protection, the State Council launched the Blue Sky Defense War initiative in July 2018, which requires that the number of days with an air quality index (AQI) < 100 accounts for more than 80% of the total number of days by the end of 2020 [20].

Aerosol monitoring is an important prerequisite for pollution management, and the main means of aerosol observation at present are in situ measurement and remote sensing. In situ measurement is mainly carried out by establishing ground stations, placing weather balloons, and using unmanned aircraft with black carbon meters [21] and particle size spectrometers [22], but these methods have disadvantages such as a small sampling range and low efficiency. After the 1960s, with the development of photoelectric detection technology, a series of ground and satellite-based optical remote sensing devices were developed [23]. Sun photometers are one of the most commonly used ground-based remote sensing instruments, they play an important role in the study of aerosol concentrations, component changes [24], pollutant monitoring [25], and climate change monitoring [26]. In aerosol optical depth (AOD) measurements, compared with satellites, sun photometers can avoid the errors introduced by aerosol, surface albedo model assumptions [27], and radiation equation simplifications [28,29], as well as atmospheric scattering, which prevents some of the satellite's measured intensity from passing through the boundary layer, resulting in the satellite being poorly sensitive to near-surface aerosol inversion [30]. Therefore, many solar photometer observation networks have been established, such as the Aerosol Robotic Network (AERONET) [31], jointly established by NASA and several domestic and foreign institutions; the MEXT Sky Radiometer Network (SKYNET) in East Asia Regional Experiment (EAREX) initiated by the United Nations Environment Programme [32]; and the Sun–Sky Radiometer Observation NETwork (SONET) [33], established by the Institute of Space Information (Chinese Academy of Sciences), to evaluate and validate the satellite AOD inversion capability and guide the satellite correction of the inversion algorithm [34,35].

$PM_{2.5}$ refers to aerosol particles with sizes less than 2.5 microns [36], which are present in near-surface air and are significantly harmful to humans [37]. There are currently more than 1400 automatic air quality monitoring stations under the Chinese Ministry of Ecology and Environment, with the vast majority of these concentrated in large cities. There is a severe lack of observation carried out in rural areas [38], with the late establishment of $PM_{2.5}$ stations and the short duration of continuous observations. Therefore, several studies have established a relationship between satellite AOD observations and $PM_{2.5}$ through a data-driven approach [39,40] to obtain the full extent of $PM_{2.5}$ concentration levels. However, ground-based remote sensing validation and accuracy assessments

of satellite AOD observations are relatively inadequate, especially in regions with few stations [41], and these errors may impact $PM_{2.5}$ estimations [42]. Studying the properties of the physical laws behind the difference between AOD and $PM_{2.5}$ trends based on the existing data accuracy and the number of $PM_{2.5}$ stations can help decipher and optimize the shortcomings of statistical learning methods [43,44] and improve the accuracy of $PM_{2.5}$ inversion from AOD. Sun photometer AOD, as a suitable calibration instrument, can simultaneously solve the challenges of satellite AOD validation and $PM_{2.5}$ and AOD discrepancy rules summarization.

There is a lack of intuitive understanding regarding the variation in AOD with different components and sources of aerosols. The complexity of aerosol sources and the diversity of components in the Beijing–Tianjin–Hebei region provide suitable natural conditions for our study. Combining data collected from various ground stations, mathematical model simulations, and satellite inversions to analyze the changes in AOD, particulate matter, and meteorology during pollution episodes can help deepen our understanding of polluted weather monitoring.

In this study, AOD monitoring datasets from August 2017 to March 2019 were obtained using a ground-based CE-318 solar photometer deployed at the Gucheng meteorological station in Baoding, Hebei, China. The station is located in the Beijing–Tianjin–Hebei region, which has a high pollution concentration background, is on the pollution transmission corridor southwest of Beijing, and is important for studying the temporal evolution patterns of aerosols in the region. First, the variation characteristics of the AOD in this dataset were compared with those of the satellite inversion on hourly, daily, and monthly scales, the performance of Himawari8 and MODIS satellite AOD inversions in rural areas were quantified, and sources of uncertainty in satellite inversions were evaluated. Then, the connection and difference between sun photometer AOD and CNEMC Air Quality Site PM data were analyzed. In addition, a haze-generating–dust-transporting composite pollution event in North China in November 2018 was analyzed, and AOD changes during the pollution event were quantified, thereby providing a reference for the study of subsequent pollution events.

This paper is organized as follows. Section 2 describes the inversion principle of the sun photometer and provides a brief description of the dataset and methods used in the paper. Section 3, Part 1 shows the comparative validation results of AOD inversions from three different instruments, and Part 2 is a comparative analysis of the difference between sun photometer AOD and $PM_{2.5}$ at the national control site. Part 3 presents an analysis of one pollution event during the study period. Section 4 summarizes the main results.

2. Data and Methods

2.1. CE-318 AOD

2.1.1. CE-318 AOD Acquisition Principle

According to the Lambert–Beer law, the monochromatic direct solar power density $E(\lambda)$ measured at ground level can be expressed as:

$$E(\lambda) = E_0(\lambda) * C * \exp(-m\tau(\lambda)) \quad (1)$$

where E_0 is the solar monochromatic direct power density reaching the top of the atmosphere, C accounts for the errors due to the absorption gas and the variation in the solar-terrestrial distance, and m is the atmospheric mass number, which can be obtained from an empirical formula. The total vertical optical thickness of the atmosphere $\tau(\lambda)$ can be calculated by obtaining the magnitudes of $E(\lambda)$ and $E_0(\lambda)$ at different wavelengths.

The total vertical optical thickness $\tau(\lambda)$ of the atmosphere consists of the Rayleigh scattering optical thickness τ_r of gas molecules, the aerosol optical thickness τ_a, and the gas absorption optical thickness τ_g. The AOD at a specific wavelength in the band where water vapor absorption does not exist is:

$$\tau_a = \tau - \tau_r - \tau_{o3} \quad (2)$$

where τ_{o3} is the absorption extinction of ozone gas.

When the spectral distribution of aerosol particles satisfies the Junge distribution and the aerosol complex refraction index does not vary with wavelength, the value of the aerosol optical thickness at any wavelength can be calculated as follows:

$$\tau_a(\lambda) = \beta\lambda^{-\alpha} \quad (3)$$

where α is the Angstrom wave length index, which is inversely proportional to the particle diameter size, and β is the atmospheric turbidity coefficient. The values of these two coefficients are usually obtained by calculating the AOD values at two wavelengths, 440 and 870 nm [45,46].

2.1.2. CE-318 AOD Data Description

The sun photometer is a high-precision spectroscopic instrument that can be used to measure the direct power density of the sun and sky at different wavelengths, and, based on sun photometer irradiance data, can be used to invert the optical properties and microphysical characteristics of aerosols, such as aerosol optical depth (AOD), single-scattering ratio, and particle size [47]. The fully automated tracking and scanning sun photometer model CE-318 (manufactured by CIMEL, Paris, France) was used, which was installed between August 2017 and March 2019 at the Gucheng meteorological observation site, 110 km southwest of Beijing, at a latitude and longitude of 115.734°E, 39.149°N, and an altitude of 20 m. The CE-318 sun photometer has eight bands. The spectral channels are 340, 380, 440, 500, 670, 870, 1020, and 1640 nm, and the measurement time resolution is 15 min. After standardized calibration and cloud screening, the AOD was inverted using the ASTPW in software with new calibration coefficients [48]. The data quality of the AOD is influenced by the hardware design, calibration method, and identification of clear sky conditions [49]. Relevant instrument parameters, calibration methods, data acquisition, and processing systems were provided by [31]. Specific cloud screening and quality control algorithms were obtained from [50]. The AOD product used in this study was at 500 nm, and the data uncertainty was typically less than 0.01 [47].

2.2. Satellite Data

2.2.1. AHI AOD

Himawari 8 is a geostationary orbit satellite (located at 140°E) that has been operated by the Japan Meteorological Agency (JMA) since July 2015. The satellite carries a multi-wavelength imager called the Advanced Himawari Imager (AHI), covering eastern Asia and the western Pacific, Australia, and nearby regions [51]. The detection bands include three visible channels, three near-infrared channels, and 10 infrared channels, with increased data products, improved spatial and temporal resolution, and the ability to synthesize color images compared with the five channels of the Himawari 7 satellite [51,52]. Currently, Himawari 8 offers two aerosol optical thickness data products, Level 2 (L2) and Level 3 (L3), both of which have a spatial resolution of 5 km [53,54]. Level 2 has a temporal resolution of 10 min, and Level 3 data have an optimal temporal resolution of 1 h [55]. The L2 data use an inversion algorithm common to multiple sensors, which first measures the error due to the uncertainty of the surface reflectance of different channels to select the best aerosol inversion channel. Then, it filters out cloudy pixels using the unbiased cloud detection algorithm [56] and spatial and temporal variations. The gas correction is then applied to the observed top-of-atmosphere (TOA) flux of the selected channel, finally minimizing the objective function to obtain several aerosol parameters, including AOD, and further inverting the single-scattering albedo and Ångström index [57]. L3 uses an hourly combination algorithm based on L2 to further remove the effect of cloud contamination and to interpolate the missing data [58]. The Level 2 version 030 aerosol dataset at 500 nm [57] from August 2017 to March 2019 was used in this study; a description of this dataset can be found at: https://www.eorc.jaxa.jp/ptree/documents/Himawari_Monitor_Aerosol_

Product_v8a.pdf (accessed on 17 June 2022). Necessary filtering was performed on the AOD data using cloud information, quality flag, etc.

2.2.2. MODIS AOD

The National Aeronautics and Space Administration (NASA) launched the first morning satellite, Terra, and the first afternoon satellite, Aqua, of the Earth Observing System (EOS) in December 1999 and May 2002, respectively, with MODIS (Moderate Resolution Imaging Spectroradiometer) as one of the main sensors onboard [59]. The sensor has a spectral range from 400 nm to 1440 nm in 36 bands. The MODIS joint Multi-Angle Implementation of Atmospheric Correction (MAIAC) algorithm inversion of the MCD19A2 version 6 with a spatial resolution of 1 km for the aerosol optical thickness product was used. Unlike conventional orbit-based processing, MAIAC re-grid plots the MODIS-measured light intensity data onto a fixed grid at a 1 km resolution so that the AOD for each grid can be retrieved individually, similar to a geostationary satellite, meaning that data from Terra and Aqua can be processed together as for a single sensor. At the same time, MAIAC takes advantage of the fact that surface changes are very slow relative to aerosol changes, to separate the surface and aerosol signals in time [60]. The MCD19A2 AOD product was originally inverted in the MODIS blue band (B3 470 nm); this product also provides the green band (B4 550 nm) AOD calculated from aerosol model spectral data [61]. The AOD product at 470 nm was used in this study and AOD QA screening was performed, similar to that performed for the AHI.

2.3. Other Data

For the comparison of AOD and $PM_{2.5}$ in Section 3.2 and the analysis of pollution events in Section 3.3, the hourly PM data from one of the China National Environmental Monitoring Centre (CNEMC) air quality sites (Baoding, Huadian II site) was used, which has a longitude and latitude of 115.5223°E and 38.8957°N. This station can conduct continuous monitoring 24 h a day. In addition, to study the effects of changing meteorological conditions on AOD and PM during pollution events, ERA-5hourly wind speed (wind, m/s), boundary layer height (BLH, m), relative humidity (relative humidity, %), and other meteorological parameters with a spatial resolution of approximately 0.4° were also used. ERA-5 is the fifth generation ECMWF (European Centre for Medium-Range Weather Forecasts) atmospheric reanalysis of the global climate [62].

2.4. Temporal Window Selection

Due to the differences in hardware settings and inversion algorithms, there are different spatial and temporal resolutions between satellite and ground-based AOD. Furthermore, the lower atmosphere is homogeneous due to turbulence and convection, so the satellite and ground-based AOD have to be matched appropriately before subsequent processing and analysis [63]. It is especially important to select a suitable spatio-temporal window, as the correlation coefficient decreases with the window size, while the number of matches increases with it [64]. In this study, satellite ground pixels using different spatial window sizes (d) centered on the location of the Gucheng site were extracted; then, the satellite and ground-based data were averaged separately with different time windows (Time); and, finally, using CE-318 data as a reference, the root-mean-square error (RMSE), mean relative error (MRE), squared correlation coefficient (R^2), and matching number (N) for the satellites data under different spatial and temporal windows were calculated (the formulae for RMSE, MRE, and R^2 are shown in the Supplementary Material). N denotes the number of CE-318 AOD measurements that can match satellite observations collocated within the spatial and temporal neighbor of CE-318 measurements. As shown in Tables 1 and 2, after weighing R^2, RMSE, and N, $d \leq 3$ pixels and time ≤ 7 min were chosen as the spatio-temporal window for AHI AOD equilibrium, and $d \leq 3$ pixels and time ≤ 10 min were chosen as the spatio-temporal window for MODIS AOD equilibrium. To check if the small time window has caused an insufficient number of N, we also try a large temporal window

of time ≤ 60 min during MODIS data validation by sun photometer. As shown in Figure S3, the number of matched N increased from 429 to 539 and R decreased from 0.97 to 0.96, comparing to a window of 10 min. The topographic map of Beijing, Tianjin and Hebei region and the related stations are shown in Figure 1.

Table 1. Sun photometer ground verification results for AHI (Advanced Himawari Imager) AOD with different combinations of time and space screening; the bold font in the table is the spatio-temporal window we selected.

	Time ≤ 2 Min			Time ≤ 5 Min			Time ≤ 7 Min			Time ≤ 10 Min			Time ≤ 20 Min		
	N	**R^2**	**RMSE**	**N**	**R^2**	**RMSE**	**N**	**R^2**	**RMSE**	**N**	**R^2**	**RMSE**	**N**	**R^2**	**RMSE**
d = 1 pixel	426	0.865	0.145	919	0.840	0.164	1078	0.840	0.161	1215	0.840	0.161	1759	0.833	0.163
d ≤ 3 pixels	1002	0.808	0.174	2533	0.790	**0.183**	**2937**	**0.787**	0.183	3267	0.780	0.185	4183	0.782	0.184
d ≤ 6 pixels	1304	0.805	0.175	3425	0.786	0.185	3955	0.781	0.187	4334	0.782	0.188	5256	0.782	0.188
d ≤ 12 pixels	1483	0.793	0.182	3959	0.774	0.194	4558	0.769	0.195	4907	0.766	0.199	5776	0.769	0.198

Table 2. Sun photometer ground validation results for MODIS (Moderate Resolution Imaging Spectroradiometer) AOD with different combinations of temporal and spatial screening, The bolded font in the table is the spatio-temporal window we selected.

	Time ≤ 2 Min			Time ≤ 5 Min			Time ≤ 7 Min			Time ≤ 10 Min			Time ≤ 20 Min		
	N	**R^2**	**RMSE**	**N**	**R^2**	**RMSE**	**N**	**R^2**	**RMSE**	**N**	**R^2**	**RMSE**	**N**	**R^2**	**RMSE**
d = 1 pixel	89	0.953	0.170	245	0.957	0.177	342	0.956	0.180	392	0.949	0.177	456	0.942	0.179
d ≤ 3 pixels	100	0.954	0.156	270	0.955	0.170	376	0.955	0.177	**429**	**0.949**	**0.173**	497	0.939	0.185
d ≤ 6 pixels	107	0.955	0.153	287	0.953	0.170	397	0.923	0.187	451	0.924	0.182	525	0.918	0.192
d ≤ 12 pixels	108	0.956	0.153	293	0.953	0.169	407	0.924	0.190	463	0.925	0.184	539	0.918	0.194

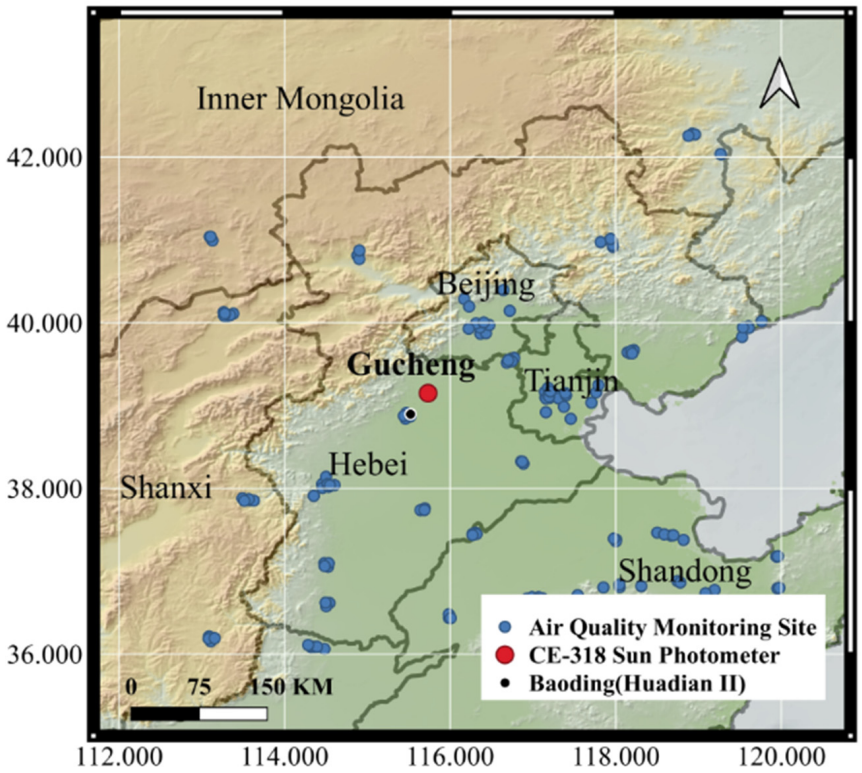

Figure 1. Topographic map of Beijing–Tianjin–Hebei region where the horizontal and vertical coordinates are the latitude and longitude, respectively. The red dot represents the sun photometer station Gucheng, the black dots represent the closest China National Environmental Monitoring Centre (CNEMC) air quality site to Gucheng (Baoding (Huadian II)), the blue dots represent the others CNEMC air quality site, and the solid gray line represents the provincial boundary.

3. Results and Discussion

3.1. Comparison and Validation of AHI, MODIS, and CE-318 AOD Inversions

In order to understand the characteristics and differences between the CE-318 solar photometer (hereinafter referred to as CE-318), AHI, and MODIS AOD on daily, monthly, and seasonal scales, a time-series comparison of the daily, monthly, and seasonal averages of the three was conducted during the observation period. As shown in Figure 2a, the daily average variation ranges of CE-318, AHI, and MODIS AOD at the Gucheng meteorological station were 0.05–3.57, 0.01–2.25, and 0.02–2.91, respectively. The overall daily average variation trends of the three were consistent, although the satellites underestimated the AOD to a certain degree on some days with high AOD. AHI AOD in general has a consistent monthly average trend with CE-318, but, on average, it is 32.7% lower. The large difference between AHI and CE-318 AOD in March 2018 and February 2019 may be related to an error in the radiative transfer model assumptions with respect to the aerosol phase function [65]. The monthly average agreement between MODIS and CE-318 is generally better than that between AHI and CE-318. It is noteworthy that in June and July 2018, both satellites showed large deviations from the daily and monthly average AOD of CE-318, which was mainly due to the frequent cloudy weather at the Gucheng site during that period, resulting in little available data after cloud screening by the satellite. As shown in the seasonal average trends in Figure S1, CE-318 AOD showed high spring and summer and low autumn and winter values, and the high value of AOD in spring may be related to the frequent dust activities in the Beijing–Tianjin–Hebei region. In summer, the increased burning of agricultural biomass in North China, as well as the secondary transformation of gaseous pollutants under high humidity conditions and the hygroscopic growth of newly generated inorganic salts, lead to an increase in AOD [66]. As the Gucheng site is in a rural area with few residents, the increase in AOD due to coal burning in winter is not significant. The mean AOD of AHI in all seasons was lower than that of CE-318 and MODIS, even though the underestimation of AOD in version 1.0 was fixed in version 2.1 [63]. The mean AOD values of MODIS in winter and summer were lower than those of CE-318, and the values in spring and autumn were higher than those of CE-318. In general, MODIS and AHI were able to reflect the daily, monthly, and seasonal variations of CE-318 AOD to some extent, and the consistency of MODIS was superior to that of AHI.

To quantitatively assess the level of accuracy of the AHI and MODIS loads on the aerosol optical depth (AOD) inversions, 2937 AHI and CE-318 AOD inversion pairs and 429 MODIS and CE-318AOD inversion pairs between August 2017 and March 2019 were acquired. The difference in the number of matches between the two is mainly because of the difference in temporal resolution between the polar-orbiting and synchronous satellites. The spatially and temporally collocated data are shown in Figure 2b,c. The black dashed line is the y = x function, and the black solid line is the linear regression of the corresponding scatter. The colored bars indicate the probability density distribution of the corresponding satellite CE-318 pairs. It can be seen that AHI, MODIS, and CE-318 AOD all show good agreement, although MODIS uses the AOD at 470 nm, which performs better than AHI in general; MODIS has a higher correlation coefficient R (0.97) than AHI (0.89); and the root-mean-square error (RMSE: 0.17) and the mean relative error (MRE: −5.57%) are smaller than the AHI AOD (RMSE: 0.18, MRE: 14.96%), similar to the validation results [27,67]. This may be due to the difference in sampling angle between geostationary and polar orbiting satellites [65], in addition, the higher spatial resolution [55,68] and better spectral setup [69] of MODIS compared with AHI may also have an impact on the results. Overall, AHI tends to underestimate AOD (MRE: 14.96%), while MODIS tends to overestimate AOD (−5.57%), and this bias, combined with the slope of the linear regression (AHI: 0.93, MODIS: 1.24), is judged to be likely due to errors in aerosol model estimation [54,70]. The intercepts of both MODIS and AHI are relatively small, −0.05 and −0.01, respectively, indicating that both are relatively accurate estimates of surface reflectance [71]. To exclude the effect of different matching numbers N, we calculated the daily average AOD scatter comparisons between AHI and MODIS with sun photometer separately, and the results

are presented in Figure S2; there was no significant difference from the previous results. Figure 3a,b show the deviations between AHI, MODIS, and CE-318 AOD, respectively, varying by different AOD value ranges. It can be seen that the average deviations of AHI and CE-318AOD are positive, and the average deviation is small (below 0.1) in most cases, even close to 0 in many cases. In contrast, the negative deviations between MODIS and CE-318AOD increase with increasing AOD, indicating that the overestimation of AOD by MODIS is more pronounced when AOD increases. Both quartile boxes tend to increase with increasing AOD, indicating that the larger the AOD, the higher the dispersion of the data [63]. Figure 3c,d show the deviations between AHI, MODIS, and CE-318 AOD, respectively, varying by different Ångström index Alpha value ranges. AHI has a smaller mean deviation from CE-318 at a larger aerosol particle size and a medium particle size (Alpha < 1.4), and a positive deviation from CE-318 at a smaller aerosol particle size (Alpha > 1.4). The negative mean deviation of MODIS from CE-318 tends to increase with a decreasing particle size.

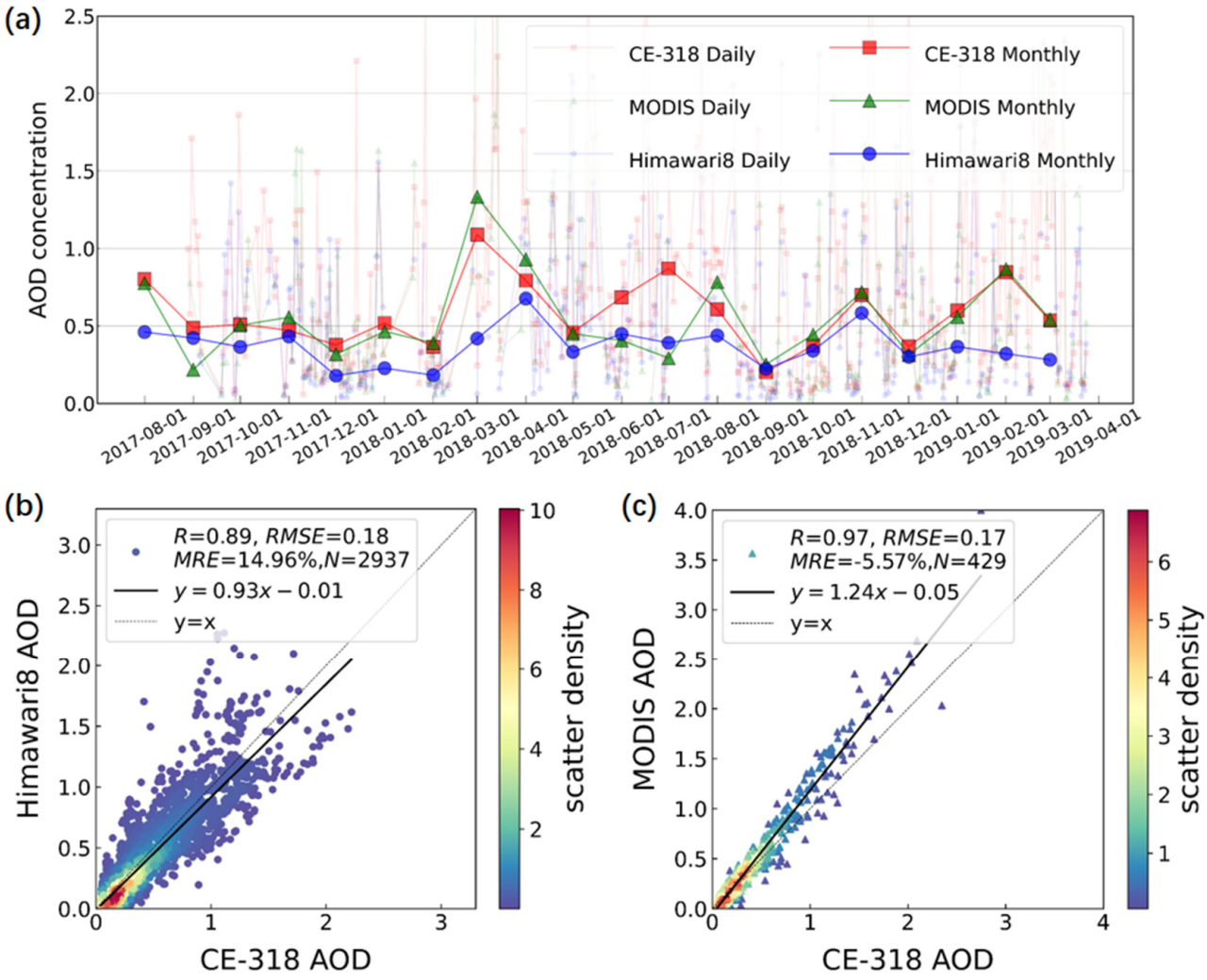

Figure 2. (**a**) Daily and monthly averaged time series of the sun photometer AOD, AHI AOD, and MODIS AOD at the Gucheng site from August 2017 to March 2019. The AHI AOD inversion at 500 nm (**b**) and the MODIS AOD inversion at 470 nm (**c**) were validated by sun photometer AOD at 500 nm at the Gucheng site from August 2017 to March 2019. Note that the original AOD measurements of the sun photometer are matched with collocated satellite ground pixels within a spatial and temporal window in (**b**,**c**).

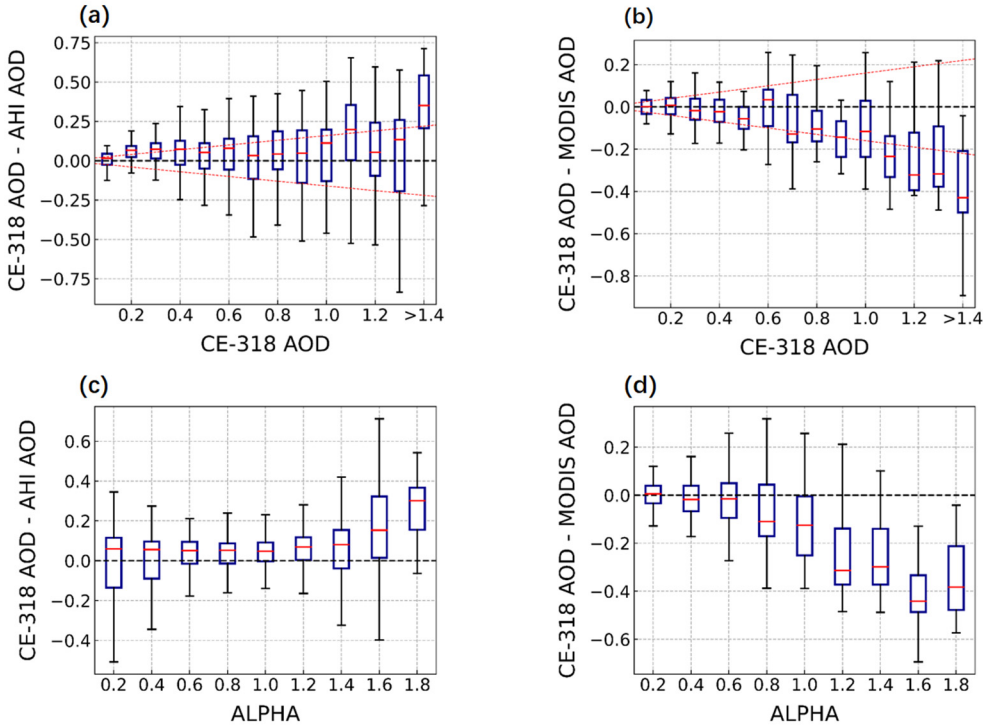

Figure 3. Box plot of the error between AHI and sun photometer AOD with respect to the size of AOD from August 2017 to March 2019 (**a**); the error between MODIS and sun photometer AOD with respect to the size of AOD (**b**); the error between AHI and sun photometer AOD with respect to the Ångström index Alpha (**c**); the error between MODIS and sun photometer AOD with respect to the Ångström index Alpha (**d**). The dark blue boxes represent the upper and lower quartiles, the black line represents the upper and lower edges of the data, and the red horizontal line inside the box represents the data mean. The red dashed line represents the envelope EE of the expected error.

The MAIAC MODIS AOD products have kept the original overpass time information from different orbits for each ground pixel. We presented the histogram of overpass time for the matched satellite AOD measurements from Terra and Aqua in Figure S5. Although Terra and Aqua overpass at the local time of 10:30 and 13:30, respectively, but still with large time spans (up to 2 h) before and after. To evaluate the accuracy level of AHI and MODIS AOD inversions at different times of the day, the daytime hours (8 a.m.–6 p.m.) were divided into three periods: 8 a.m.–11 a.m. in the morning, 11 a.m.–2 p.m. in the noon period, and 2 p.m.–6 p.m. in the afternoon. The scattered points in Figure 2b,c are processed in three periods, and the results are displayed in Figures 4 and 5. We can see that the correlation coefficients of MODIS in the three periods (R = 0.97–0.98) are greater than those of AHI (R = 0.88–0.91); the MRE is −4.77–7.82%, which is smaller than that of AHI (MRE = 9.35–16.90%); the RMSE is 0.17–0.20, comparable to that of AHI (RMSE = 0.15–0.23); and the number of matches is N = 43–311, which is smaller than AHI (N = 626–1260). Although the consistency of MODIS matches with CE-318 at different times of the day is better than that of AHI, the number of MODIS AOD matches is concentrated in the noon period, which is 4.1 and 7.2 times higher than at midday and in the afternoon, respectively, accounting for 72.4% of the total number of matches. Therefore, the AHI data can be used as a complement to MODIS in the morning and afternoon. The slope of the AHI is 0.67 in the morning and 0.91 and 1.14 in the noon and afternoon, respectively, which may be due to the variation in the uncertainty with time of day caused by the aerosol model assumptions in the satellite inversion. AHI AOD shows an underestimation of AOD compared with CE-318 AOD in all three periods of the day (MRE: 9.35–16.90%), with the most severe underestimation in the noon period (MRE: 16.90%). The MODIS slopes of 1.36, 1.18, and 1.34 in the morning, noon, and afternoon periods, respectively, may be caused by

an overestimation of the aerosol model, which often corresponds to an underestimation of surface reflectance (intercept: −0.03–(−0.14)) [70]. Compared with CE-318, MODIS shows an overestimation of AOD in the morning and noon periods (MRE: −4.77–7.62%), and an underestimation of AOD in the afternoon (MRE: 7.82%). The errors of slope and intercept of the two satellites are smaller in the noon period than in the other two periods, which may be related to the daily variation in solar zenith angle and scattering angle [64].

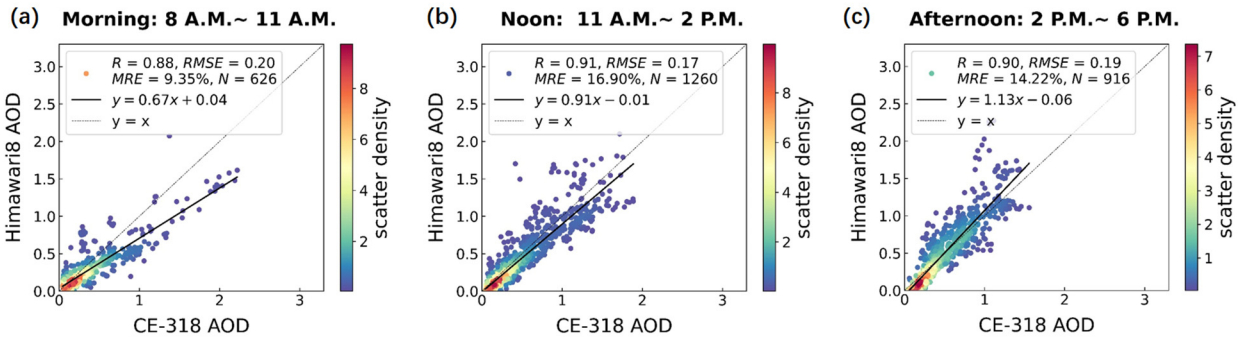

Figure 4. AHI AOD inversions were evaluated at different times of the morning (**a**), noon (**b**), and afternoon (**c**) using the Gucheng sun photometer AOD as a standard.

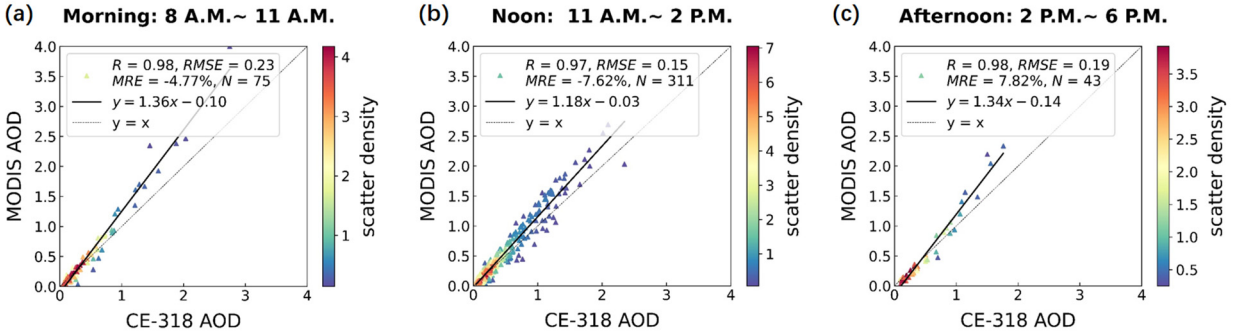

Figure 5. MODIS AOD inversions were evaluated at different times of the morning (**a**), noon (**b**), and afternoon (**c**) using the Gucheng sun photometer AOD as a standard.

The scatter comparisons of AHI, MODIS, and CE-318 AOD for different seasons are shown in Figures 6 and 7. Consistent with the findings of the total scatter comparison and the scatter comparison of different periods during the day, the correlation coefficient (R = 0.97–0.98) of MODIS is greater than that of AHI (R = 0.89–0.90); the mean relative error (MRE = 37.47–41.82%) is smaller than that of AHI (MRE = 24.34–35.10%); and the root-mean-square error (RMSE = 0.13–0.25) is comparable to that of AHI (0.15–0.25), with better performance. The correlation coefficients of AHI and CE-318 did not differ significantly in different seasons. In autumn, the linear fit of AHI scatter was close to the Y = X line; the intercept of AHI in winter was higher than in other seasons, which might be related to the surface albedo error caused by the change in surface vegetation and the contamination of snow in winter in Gucheng [53]; and in summer, the slope of AHI deviated from the ideal value the most at 0.77, and the RMSE and MRE were also higher at 0.25 and 30.94%, respectively, which is probably related to the fact that Gucheng aerosols are mostly fine particles in summer; as shown in Figure S4, the large inversion error of AHI for fine modal particles leads to the underestimation of the AHI AOD [72].The slope of MODIS in different seasons ranges from 1.19 to 1.31, and the inversion results do not correlate well with the seasonal changes. In addition, the lower matching number of MODIS in summer and AHI in winter and summer may be related to the strict screening of rain and snow. The albedo and aerosol models need to be refined for different seasons and time periods in the inversion, and the effects of factors such as AOD size, particle size, and solar zenith angle variations should be fully considered.

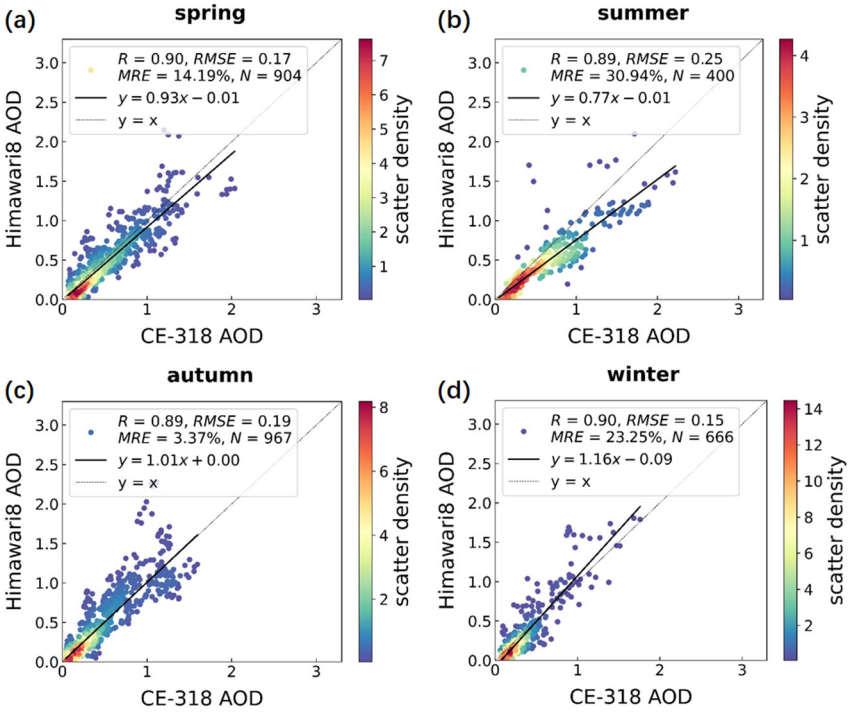

Figure 6. AHI AOD inversions were evaluated for the different seasons of spring (**a**), summer (**b**), fall (**c**), and winter (**d**) during the August 2017 to March 2019 period, using the Gucheng sun photometer AOD as a benchmark.

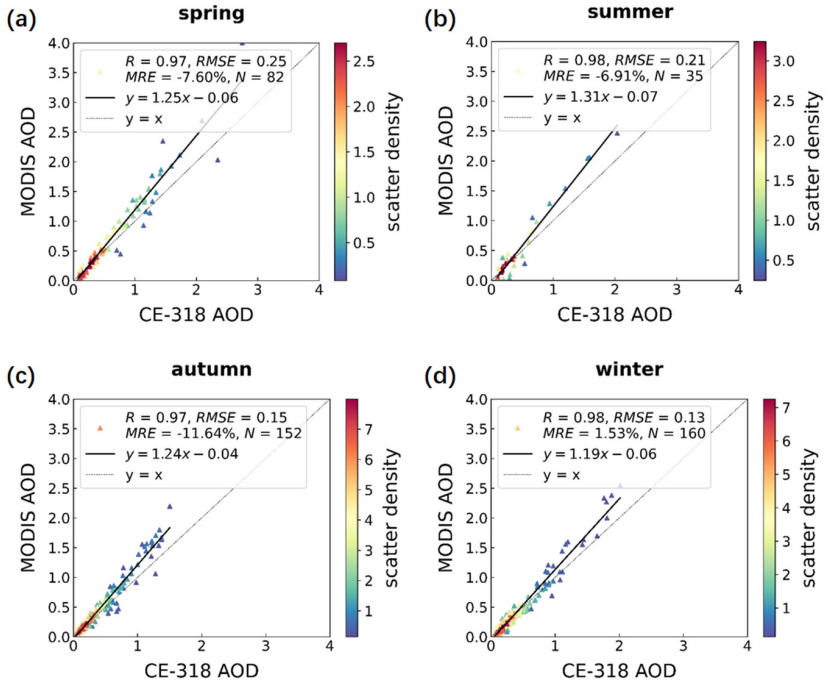

Figure 7. MODIS AOD inversions were evaluated for the different seasons of spring (**a**), summer (**b**), fall (**c**), and winter (**d**) during the August 2017 to March 2019 period, using the Gucheng sun photometer AOD as a benchmark.

3.2. Comparison of CE-318 AOD and $PM_{2.5}$ of CNEMC Air Quality Site Validation

The AOD on the pollution transmission channel in the rural site near Beijing is large and rapidly changing. Studying the association and difference between AOD and $PM_{2.5}$ in this area can provide a valuable reference for our subsequent inversion of $PM_{2.5}$ using AOD.

The Gucheng AOD data for the same hour on different days and for the same month on different days were averaged to obtain the results shown in Figure 8a,d, respectively. In the same way, the time series plots of the $PM_{2.5}$ concentration at the national control site in Figure 8b,e, the Ångström index Alpha of Gucheng AOD, the Pearson correlation coefficient R of $PM_{2.5}$ and AOD, and the $PM_{2.5}$/AOD hourly average and monthly average were obtained in Figure 8c,f, To exclude the effect of AOD and $PM_{2.5}$ not being in the same location. We plotted a comparison of the hourly and monthly averages of AHI AOD for Gucheng and Baoding in Figure S7, which are very similar. So, we ignore the difference in $PM_{2.5}$ between Baoding (Huadian II) and Gucheng.

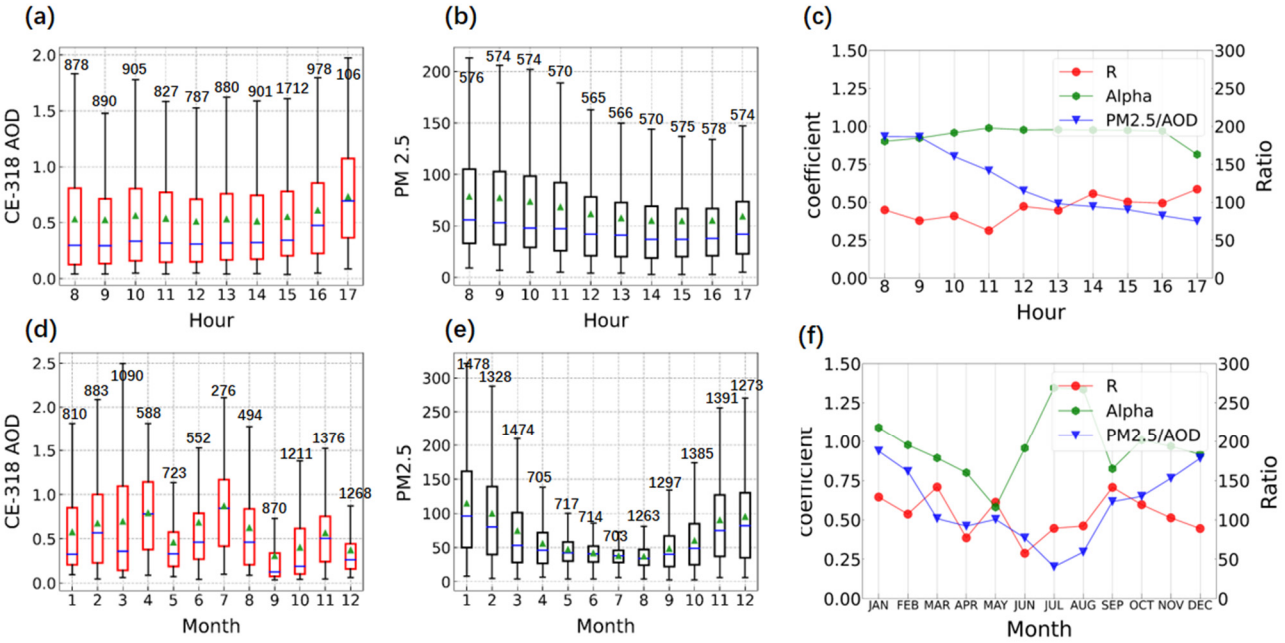

Figure 8. Daily variation boxplot of the solar photometer AOD (**a**) in Gucheng and $PM_{2.5}$ (**b**) at the CNEMC(China National Environmental Monitoring Centre) air quality site in Baoding (Huadian II) during the August 2017 to March 2019 period, and seasonal variation boxplot (**d**,**e**).The red and black boxes represent the upper and lower quartiles, the black line represents the upper and lower edges of the data, and the blue horizontal line inside the box represents the data median, the green triangle indicates the data mean. Correlation coefficient R2 of AOD and $PM_{2.5}$, Ångström exponent Alpha of AOD, $PM_{2.5}$/AOD daily variation (**c**), and seasonal variation (**f**).

As shown in Figure 8a, The CE-318 AOD in Gucheng is almost constant from 8:00 a.m. to 2:00 p.m., with a mean value of 0.530, and rises slowly after 2:00 p.m., finally reaching 0.732. Elevated AOD in the afternoon may be associated with secondary aerosol formation [73]. The $PM_{2.5}$ concentrations in Baoding (Huadian II) were high in the morning and evening (above 0.9 $\mu g/m^3$) and low in the noon period (below 0.4 $\mu g/m^3$), as shown in Figure S6. The daily variation of $PM_{2.5}$ may be influenced by human commuting and boundary layer height [74]. As shown in Figure 8d,e, AOD is high in summer and low in winter, the Seasonal changes of $PM_{2.5}$ show opposite trends. Such opposite trends are consistent with previous findings [75,76], possibly related to the vertical inhomogeneity of aerosol distribution [75] leading by the emission patterns such as biomass burning in summer [76] and coal burning in winter [77], meteorological variations such as relative humidity [78] and boundary layer height variations [79].

The relationship between AOD and $PM_{2.5}$ is influenced by the aerosol type, optical properties, vertical distribution, particle size spectrum, ambient relative humidity, climate of the observation site, and other factors. The value of $PM_{2.5}$/AOD derived from chemical transport models is commonly used to estimate $PM_{2.5}$ by multiplying the satellite AOD [74,80]. As shown in Figure 8c, the correlation coefficient between AOD and $PM_{2.5}$

decreases and then increases, with a mean value of 0.46. The reason for the variation in $PM_{2.5}$/AOD and correlation coefficient R in the Gucheng is mainly that the boundary layer height is low at around 8:00 a.m., and pollutants are concentrated near the ground, so the correlation between AOD and $PM_{2.5}$ is high. From 8:00 a.m. to 11:00 a.m., with the gradual increase of the boundary layer height, the AOD, which characterizes the concentration of the entire atmospheric column, inevitably differs from the near-surface $PM_{2.5}$, and the correlation coefficient between them decreases. After 11:00 a.m., until 5 pm, the $PM_{2.5}$ concentration kept transmitting upward and the correlation coefficient between $PM_{2.5}$ and AOD started to increase again. $PM_{2.5}$/AOD shows a decreasing trend throughout the day, with the highest value of 186.4 occurring at 8 a.m. and the lowest value of 74.98 occurring at 5 p.m. For the seasonal variations shown in Figure 8f, the correlation coefficient between AOD and $PM_{2.5}$ was highest in autumn at 0.61 and lowest in summer at 0.40. This may be related to the seasonal variation of boundary layer height. $PM_{2.5}$/AOD showed the lowest in summer and highest in winter, which is due to the opposite seasonality of AOD and PM concentrations. It can be seen that the relationship between $PM_{2.5}$ and AOD is affected by seasons and daily variations, and these factors should be taken into account when inverting $PM_{2.5}$.

The Ångström index Alpha is an important parameter when characterizing the particle size of aerosols, with natural aerosols having larger particles [81], while anthropogenic aerosols tend to have finer particles. As shown in Figure 8c, the Alpha at the Gucheng site remained around 0.9 for most of the day, with little significant variation. For the seasonal variation in Figure 8e, the mean Alpha is 0.975, which is high in summer (1.4) and low in spring (0.6) and is related to the fine particles generated by agricultural burning in summer, while dust brings a large amount of coarse particulate matter in spring. In addition, we found that, for seasonal variations, the trends in Alpha and AOD are relatively close, indicating that particle size is an important factor affecting the aerosol extinction coefficient [82].

All the above results are obtained by ignoring the $PM_{2.5}$ spatial differences between Gucheng and Baoding(Huadian II), and more detailed analyses are needed to set up stations at the same locations.

3.3. Analysis of a Pollution Event in Late Autumn in the North China Plain

To gain an intuitive understanding of the changes in AOD during the occurrence of different types of polluted weather and to improve future warning capabilities for heavily polluted weather, a representative complex pollution event in North China during the period from 23 November 2018 to 30 November 2018 was analyzed. During the observation period, the weather conditions in North China experienced a haze-to-dust transition, which was prompted by cold air from the northwest desert region on 27 November [83]. AOD observations from CE-318, MODIS, and AHI at the Gucheng weather station during this period, and daily averaged AOD observations from the Himawari 8 satellite in the Beijing–Tianjin–Hebei region were extracted, with the results displayed in Figures 9b and 10. In addition, the hourly PM observations from the nearest CNEMC air quality site (Baoding Huadian II) in Gucheng during this period, and the meteorological data from the ERA-5 in Gucheng were selected for further analysis of the pollution events during the observation period, as shown in Figures 9a and 10.

It can be seen that the satellite and ground-based AOD and the ground-based AOD and PM at the national control site have similar trends, although there are some spatial location differences between the sun photometer and the national control site, and the previously discussed opposite daily trends of AOD and PM can be reflected here. $PM_{2.5}/PM_{10} < 0.4$ was defined as a dusty day [84], and this pollution event can be roughly divided into four stages in time: haze, local pollution and dust mixing, dusty backflow, and pollution transmission.

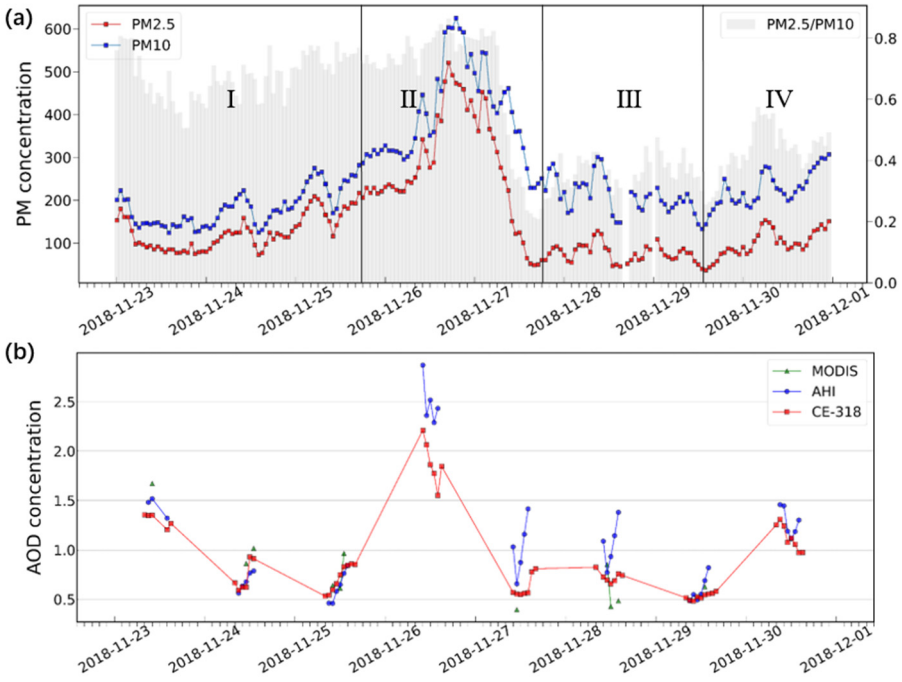

Figure 9. (**a**) Comparison of hourly $PM_{2.5}$ and PM_{10} concentrations and $PM_{2.5}/PM_{10}$ time series at the CNEMC air quality site in Baoding (Huadian II) from 23 to 30 November 2018. (**b**) Comparison of hourly time series of Gucheng sun photometer, AHI, and MODIS AOD from 23 to 30 November 2018.

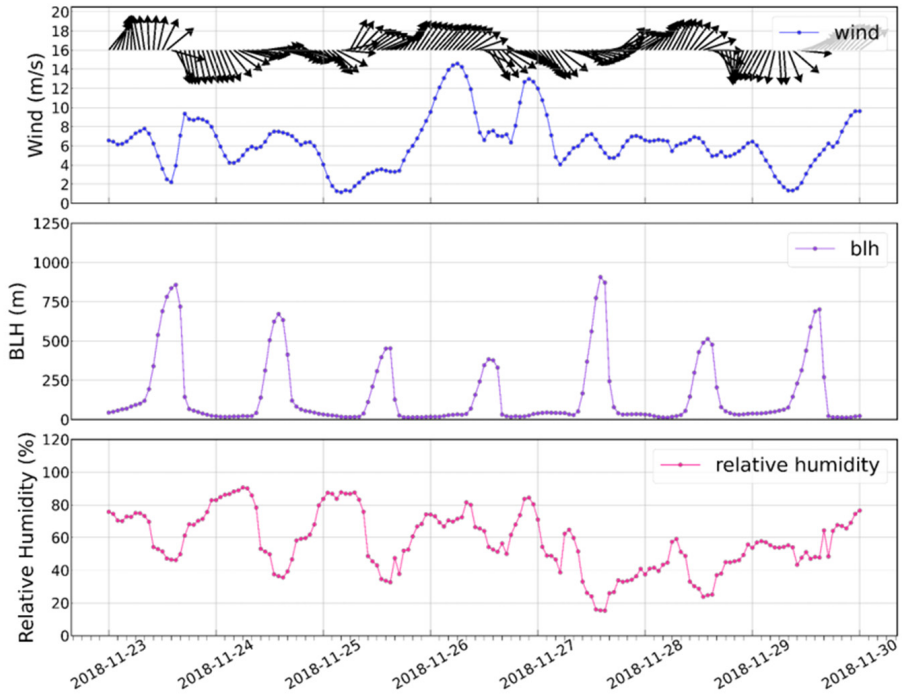

Figure 10. ERA-5 meteorological data including wind direction, wind speed, boundary layer height, surface relative humidity at Gucheng from 23 to 30 November 2018. Note that wind variables are at an altitude level of 925 hPa.

Phase I (haze): from 23 November 4 p.m. to 25 November at 6 p.m., due to the high relative humidity during this period and the continuous decrease in wind speed and boundary layer height, resulting in increasing pollution near the ground. $PM_{2.5}$ concentrations increased slowly during this period, but AOD did not change significantly.

Phase II (local pollution and dust mixing): from 25 November at 6 p.m. to 26 November to 6 p.m., the boundary layer height continues to decrease and pollution continues to increase, AOD reached a peak of 2.2 at 10 a.m. on 26 November. Since the AOD observation can only be performed during the daytime, the change in AOD after 3:00 p.m. on 26 November could not be obtained. Starting from 6 p.m. on 26 November, the wind direction shifted to the northwest, the wind speed and boundary layer height started to rise, relative humidity decreased, and PM concentrations increased rapidly. In combination with the bimodal structure of PM concentrations in Shijiazhuang during this period, we suggest that this may have been caused by the local emission of pollutants and the mixing of dust near Baoding and Shijiazhuang. Thereafter, the $PM_{2.5}/PM_{10}$ concentrations decreased to below 0.4 and AOD decreased to approximately 0.6 with the arrival of dust days, and the air quality improved substantially. Phase III (dust backflow): the $PM_{2.5}/PM_{10}$ concentrations increased again after 6:00 p.m. on 27 November. Combining the spatial distribution of the satellite AOD with the wind field data (Figure S8), it can be surmised that this was probably caused by the dust backflow [85]. At 1 p.m. on 29 November, accompanied by a north wind, the PM concentration dropped to the lowest value during the observation period, and the weather condition in the Gucheng area further improved. Our photometer also detected an increase in AOD on 28 November and a decrease in AOD on 29 November, with daily averages of 0.72 and 0.53, respectively. Phase IV (pollution transport): as shown in Figure S9, the southwest wind brought the high AOD from the south of Hebei to Gucheng, and the meteorological conditions were also favorable for pollutant generation.

The daily average spatial distribution of AHI AOD during the pollution event is shown in Figure 11, with the black star denoting the Gucheng weather stations. From 23 to 24 November, under the of northwest and north winds, the AOD in south-central Hebei dropped significantly, with most areas below 0.25, except for southern Beijing, Langfang, Gucheng, and eastern Shandong, where the AOD was around 1.0. On 25 November, under the hazy weather, the Gucheng site and the area around Handan and Hengshui in southwestern Hebei had a high AOD, reaching more than 1.25 in some areas. On 26 November, there were two areas of high AOD in northern China, one in Shanxi and northern Hebei, and the other in the Shijiazhuang–Gucheng–Beijing pollution belt, which were caused by sand and dust, and local pollution transmission, respectively. On 27 November, pollutants reached southern Hebei under the of the north wind, and Gucheng's air quality improved. On 28 November, the AOD of Gucheng rose due to the dust backflow. From 29 to 30 November, the transfer of pollution transmission channels and secondary generation of pollutants again caused the AOD of Gucheng to rise to approximately 1.3.

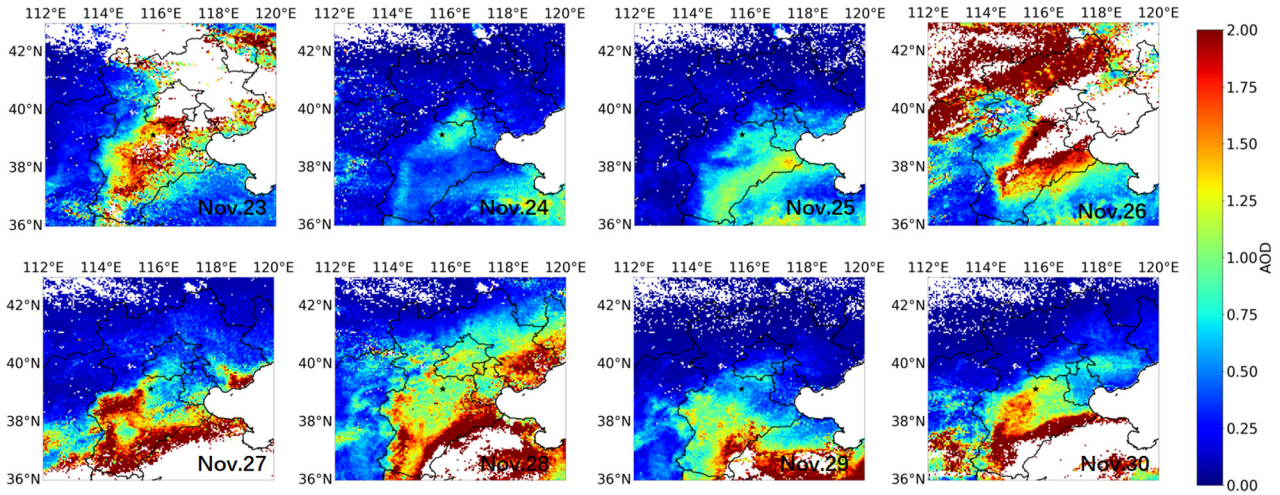

Figure 11. Daily average spatial distribution of Beijing–Tianjin–Hebei AHI AOD from 23 to 30 November 2018, with the location of Gucheng denoted by a black star.

4. Conclusions

The Beijing–Tianjin–Hebei region, as an industrial and densely populated urban agglomeration, is an area with one of the most serious levels of atmospheric aerosol pollution. At present, AOD observation studies in the Beijing–Tianjin–Hebei region usually focus on urban and suburban areas; therefore, there is a lack of analysis of long-term AOD data in the rural background areas of Beijing. First, long-term AOD observation data from the Gucheng site were used, which is 110 km away from Beijing and on the pollution transmission channel southwest of Beijing and compared the observation data with datasets of AHI and MODIS for validation. The correlation coefficient of MODIS (R = 0.97), root-mean-square error (RMSE = 0.17), mean relative error (MRE = −5.57%), and agreement with the CE-318 AOD match was better than that of AHI (R: 0.89, RMSE: 0.18, MRE: 14.96%), both overall and by season and period. The mean deviation of MODIS from CE-318 has a strong dependence on AOD size and Ångström index Alpha and is less stable than that of AHI. In addition, the inversion results of AHI and MODIS depend on the period and seasonal changes to different degrees, and the models need to be adjusted accordingly.

During the comparison between CE-318 AOD measurements in the Gucheng site and $PM_{2.5}$ observations from the CNEMC site nearby, we found significant differences in the daily and seasonal patterns of AOD and $PM_{2.5}$. $PM_{2.5}$/AOD has a decreasing trend throughout the day and reaches the lowest in summer and highest in winter. The daily variation amplitude of the correlation coefficient between $PM_{2.5}$ and AOD is much smaller than that of the seasonal variation amplitude, and a similar pattern can also be found for the Ångström index.

In the week-long analysis of pollution events, we found that, even if there are some differences in station location, the daily variation trends are different and AOD can still reflect the variation patterns of PM to some extent, which provides a reference for polluted weather monitoring in Beijing. However, due to the shortcomings of photometry and satellite passive remote sensing, the observed values of AOD can only be obtained during the daytime, which has some influence on the analysis of the daily variation in pollutants.

It should be noted that that AOD and data not in the same location may introduce errors to $PM_{2.5}$, and the relevant conclusions still need further verification. The inability of the sun photometer to achieve night-time observations and directly resolve aerosol chemical components make its use limited in stand-alone observations, meaning that it is necessary to follow up with enhanced observations using a combined aerosol lidar and mass spectrometer to analyze long-term aerosol trends and their drivers. Overall, our study has implications for understanding and improving satellite AOD inversion errors in the Beijing–Tianjin–Hebei region, analysis of the source of near-surface $PM_{2.5}$ and AOD differences in rural site near Beijing, and early warnings of heavily polluted weather based on AOD observations.

Supplementary Materials: The following supporting information can be downloaded at: https://www.mdpi.com/article/10.3390/rs14122908/s1, Text: The definition of correlation coefficient R, root mean square error RMSE, mean relative error MRE and envelope EE of the expected error; Figure S1. Seasonal averaged time series of the sun photometer AOD, AHI AOD, and MODIS AOD at the Gucheng site from August 2017 to March 2019. Figure S2. The daily average AHI AOD inversion at 500 nm and the daily average MODIS AOD inversion at 470 nm were evaluated for the period from August 2017 to March 2019, using the daily average sun photometer AOD at 500 nm at the Gucheng site as a standard. Figure S3. The MODIS AOD inversion at 470 nm were evaluated for the period from August 2017 to March 2019, using the raw sun photometer AOD at 500 nm at the Gucheng site as a standard. The spatio-temporal matching window of (a) is: Time $\leq$ 10 min, d $\leq$ 3 pixels. The spatio-temporal matching window of (b) is: Time $\leq$ 60 min, d $\leq$ 3 pixels. Figure S4. Monthly Average Change in Ångström index. Figure S5. TERRA and AQUA's overpass time distribution. For calculation purposes, the horizontal. Figure S6. Daily variation of $PM_{2.5}$ at the CNEMC (China National Environmental Monitoring Centre) air quality site in Baoding (Huadian II) during the August 2017 to March 2019 period. Figure S7. Daily variation (a) of AHI AOD in Gucheng and PM2.5 at the CNEMC (China National Environmental Monitoring Center)

air quality site in Baoding (Huadian II) during the August 2017 to March 2019 period, and seasonal variation (c). Daily variation (b) of AHI AOD in Baoding (Huadian II) and PM2.5 at the CNEMC (China National Environmental Monitoring Center) air quality site in Baoding (Huadian II) during the August 2017 to March 2019 period, and seasonal variation (d). Figure S8. In the context of the daily average AOD, the ERA-5 wind field at 2 p.m., 8:00 p.m., on 27 November 2018 and at 2:00 a.m., 8:00 a.m. on 28 November 2018, respectively. Figure S9. In the context of the daily average AOD, the ERA-5 wind field at 8:00 p.m., on 29 November 2018 and at 2:00 a.m. on 30 November 2018, respectively.

Author Contributions: Conceptualization, H.X.; Methodology, X.W.; Software, X.W.; Formal Analysis, H.X., J.Y., T.W. and X.W.; Investigation, X.W.; Resources, J.Y., T.W., Y.Z. and K.W.; Data Curation, X.W.; Writing—Original Draft Preparation, H.X. and X.W.; Writing—Review and Editing, H.X., J.Y. and T.W.; Visualization, X.W.; Supervision, H.X. All authors have read and agreed to the published version of the manuscript.

Funding: This research received no external funding.

Data Availability Statement: The data presented in this study are available on request from the corresponding author.

Acknowledgments: We acknowledge the MODIS for their effort in making the data available. We acknowledge the Meteorological Satellite Center (MSC) of the Japan Meteorological Agency (JMA) for providing Himawari-8 data. We acknowledge the surface air quality observation data from CNEMC. We acknowledge all developers for contributing to the development of the ECMWF.

Conflicts of Interest: The authors declare no conflict of interest.

References

1. Luo, X.; Bing, H.; Luo, Z.; Wang, Y.; Jin, L. Impacts of atmospheric particulate matter pollution on environmental biogeochemistry of trace metals in soil-plant system: A review. *Environ. Pollut.* **2019**, *255*, 113138. [CrossRef]
2. Brodny, J.; Tutak, M. Analysis of the diversity in emissions of selected gaseous and particulate pollutants in the European Union countries. *J. Environ. Manag.* **2019**, *231*, 582–595. [CrossRef] [PubMed]
3. Drewnick, F.; Pikmann, J.; Fachinger, F.; Moormann, L.; Sprang, F.; Borrmann, S. Aerosol filtration efficiency of household materials for homemade face masks: Influence of material properties, particle size, particle electrical charge, face velocity, and leaks. *Aerosol Sci. Technol.* **2021**, *55*, 63–79. [CrossRef]
4. Zhu, Q.; Cao, L.-M.; Tang, M.-X.; Huang, X.-F.; Saikawa, E.; He, L.-Y. Characterization of organic aerosol at a rural site in the North China Plain region: Sources, volatility and organonitrates. *Adv. Atmos. Sci.* **2021**, *38*, 1115–1127. [CrossRef]
5. Huang, R.-J.; Wang, Y.; Cao, J.; Lin, C.; Duan, J.; Chen, Q.; Li, Y.; Gu, Y.; Yan, J.; Xu, W. Primary emissions versus secondary formation of fine particulate matter in the most polluted city (Shijiazhuang) in North China. *Atmos. Chem. Phys.* **2019**, *19*, 2283–2298. [CrossRef]
6. Vione, D.; Maurino, V.; Minero, C.; Pelizzetti, E.; Harrison, M.A.; Olariu, R.-I.; Arsene, C. Photochemical reactions in the tropospheric aqueous phase and on particulate matter. *Chem. Soc. Rev.* **2006**, *35*, 441–453. [CrossRef]
7. Bellouin, N.; Quaas, J.; Gryspeerdt, E.; Kinne, S.; Stier, P.; Watson-Parris, D.; Boucher, O.; Carslaw, K.S.; Christensen, M.; Daniau, A.L. Bounding global aerosol radiative forcing of climate change. *Rev. Geophys.* **2020**, *58*, e2019RG000660. [CrossRef] [PubMed]
8. Fan, J.; Wang, Y.; Rosenfeld, D.; Liu, X. Review of aerosol–cloud interactions: Mechanisms, significance, and challenges. *J. Atmos. Sci.* **2016**, *73*, 4221–4252. [CrossRef]
9. Han, T.; Liu, X.; Zhang, Y.; Qu, Y.; Zeng, L.; Hu, M.; Zhu, T. Role of secondary aerosols in haze formation in summer in the Megacity Beijing. *J. Environ. Sci.* **2015**, *31*, 51–60. [CrossRef]
10. Peng, J.; Hu, M.; Shang, D.; Wu, Z.; Du, Z.; Tan, T.; Wang, Y.; Zhang, F.; Zhang, R. Explosive secondary aerosol formation during severe haze in the North China Plain. *Environ. Sci. Technol.* **2021**, *55*, 2189–2207. [CrossRef]
11. Wang, Z.; Akimoto, H.; Uno, I. Neutralization of soil aerosol and its impact on the distribution of acid rain over east Asia: Observations and model results. *J. Geophys. Res. Atmos.* **2002**, *107*, ACH 6-1–ACH 6-12. [CrossRef]
12. Yang, Y.; Qi, J.; Ruan, Z.; Yin, P.; Zhang, S.; Liu, J.; Liu, Y.; Li, R.; Wang, L.; Lin, H. Changes in life expectancy of respiratory diseases from attaining daily PM2.5 standard in China: A nationwide observational study. *Innovation* **2020**, *1*, 100064. [CrossRef] [PubMed]
13. Niu, B.-Y.; Li, W.-K.; Li, J.-S.; Hong, Q.-H.; Khodahemmati, S.; Gao, J.-F.; Zhou, Z.-X. Effects of DNA damage and oxidative stress in human bronchial epithelial cells exposed to PM2.5 from Beijing, China, in winter. *Int. J. Environ. Res. Public Health* **2020**, *17*, 4874. [CrossRef] [PubMed]
14. Li, M.; Mao, C. Spatial effect of industrial energy consumption structure and transportation on haze pollution in Beijing-Tianjin-Hebei region. *Int. J. Environ. Res. Public Health* **2020**, *17*, 5610. [CrossRef]

15. Quan, J.; Dou, Y.; Zhao, X.; Liu, Q.; Sun, Z.; Pan, Y.; Jia, X.; Cheng, Z.; Ma, P.; Su, J. Regional atmospheric pollutant transport mechanisms over the North China Plain driven by topography and planetary boundary layer processes. *Atmos. Environ.* **2020**, *221*, 117098. [CrossRef]
16. Wu, J.; Bei, N.; Wang, Y.; Li, X.; Liu, S.; Liu, L.; Wang, R.; Yu, J.; Le, T.; Zuo, M. Insights into particulate matter pollution in the North China Plain during wintertime: Local contribution or regional transport? *Atmos. Chem. Phys.* **2021**, *21*, 2229–2249. [CrossRef]
17. Xiao, C.; Chang, M.; Guo, P.; Gu, M.; Li, Y. Analysis of air quality characteristics of Beijing–Tianjin–Hebei and its surrounding air pollution transport channel cities in China. *J. Environ. Sci.* **2020**, *87*, 213–227. [CrossRef]
18. Dang, R.; Liao, H. Severe winter haze days in the Beijing–Tianjin–Hebei region from 1985 to 2017 and the roles of anthropogenic emissions and meteorology. *Atmos. Chem. Phys.* **2019**, *19*, 10801–10816. [CrossRef]
19. Feng, Y.; Ning, M.; Lei, Y.; Sun, Y.; Liu, W.; Wang, J. Defending blue sky in China: Effectiveness of the "Air Pollution Prevention and Control Action Plan" on air quality improvements from 2013 to 2017. *J. Environ. Manag.* **2019**, *252*, 109603. [CrossRef]
20. Yang, X.; Wang, Y.; Chen, D.; Tan, X.; Tian, X.; Shi, L. Does the "Blue Sky Defense War Policy" Paint the Sky Blue?—A Case Study of Beijing–Tianjin–Hebei Region, China. *Int. J. Environ. Res. Public Health* **2021**, *18*, 12397. [CrossRef] [PubMed]
21. Wang, J.; Liu, D.; Ge, X.; Wu, Y.; Shen, F.; Chen, M.; Zhao, J.; Xie, C.; Wang, Q.; Xu, W. Characterization of black carbon-containing fine particles in Beijing during wintertime. *Atmos. Chem. Phys.* **2019**, *19*, 447–458. [CrossRef]
22. Froyd, K.D.; Murphy, D.M.; Brock, C.A.; Campuzano-Jost, P.; Dibb, J.E.; Jimenez, J.-L.; Kupc, A.; Middlebrook, A.M.; Schill, G.P.; Thornhill, K.L. A new method to quantify mineral dust and other aerosol species from aircraft platforms using single-particle mass spectrometry. *Atmos. Meas. Tech.* **2019**, *12*, 6209–6239. [CrossRef]
23. Bilal, M.; Nazeer, M.; Nichol, J.; Qiu, Z.; Wang, L.; Bleiweiss, M.P.; Shen, X.; Campbell, J.R.; Lolli, S. Evaluation of Terra-MODIS C6 and C6. 1 aerosol products against Beijing, XiangHe, and Xinglong AERONET sites in China during 2004–2014. *Remote Sens.* **2019**, *11*, 486. [CrossRef]
24. Tegen, I.; Hollrig, P.; Chin, M.; Fung, I.; Jacob, D.; Penner, J. Contribution of different aerosol species to the global aerosol extinction optical thickness: Estimates from model results. *J. Geophys. Res. Atmos.* **1997**, *102*, 23895–23915. [CrossRef]
25. Sioris, C.E.; Abboud, I.; Fioletov, V.E.; McLinden, C.A. AEROCAN, the Canadian sub-network of AERONET: Aerosol monitoring and air quality applications. *Atmos. Environ.* **2017**, *167*, 444–457. [CrossRef]
26. Ridley, D.; Solomon, S.; Barnes, J.; Burlakov, V.; Deshler, T.; Dolgii, S.; Herber, A.B.; Nagai, T.; Neely, R., III; Nevzorov, A. Total volcanic stratospheric aerosol optical depths and implications for global climate change. *Geophys. Res. Lett.* **2014**, *41*, 7763–7769. [CrossRef]
27. Tao, M.; Wang, J.; Li, R.; Wang, L.; Wang, L.; Wang, Z.; Tao, J.; Che, H.; Chen, L. Performance of MODIS high-resolution MAIAC aerosol algorithm in China: Characterization and limitation. *Atmos. Environ.* **2019**, *213*, 159–169. [CrossRef]
28. Ceballos, J.C.; Bottino, M.J.; De Souza, J.M. A simplified physical model for assessing solar radiation over Brazil using GOES 8 visible imagery. *J. Geophys. Res. Atmos.* **2004**, *109*, D02211. [CrossRef]
29. Song, Z.; Fu, D.; Zhang, X.; Han, X.; Song, J.; Zhang, J.; Wang, J.; Xia, X. MODIS AOD sampling rate and its effect on PM2.5 estimation in North China. *Atmos. Environ.* **2019**, *209*, 14–22. [CrossRef]
30. Martin, R.V. Satellite remote sensing of surface air quality. *Atmos. Environ.* **2008**, *42*, 7823–7843. [CrossRef]
31. Holben, B.N.; Eck, T.F.; Slutsker, I.A.; Tanre, D.; Buis, J.P.; Setzer, A.; Vermote, E.; Reagan, J.A.; Kaufman, Y.J.; Nakajima, T.; et al. AERONET—A Federated Instrument Network and Data Archive for Aerosol Characterization. *Remote Sens. Environ.* **1998**, *66*, 1–16. [CrossRef]
32. Campanelli, M.; Estellés, V.; Tomasi, C.; Nakajima, T.; Malvestuto, V.; Martínez-Lozano, J.A. Application of the SKYRAD Improved Langley plot method for the in situ calibration of CIMEL Sun-sky photometers. *Appl. Opt.* **2007**, *46*, 2688–2702. [CrossRef]
33. Li, Z.; Xu, H.; Li, K.; Li, D.; Xie, Y.; Li, L.; Zhang, Y.; Gu, X.; Zhao, W.; Tian, Q. Comprehensive study of optical, physical, chemical, and radiative properties of total columnar atmospheric aerosols over China: An overview of Sun–Sky Radiometer Observation Network (SONET) measurements. *Bull. Am. Meteorol. Soc.* **2018**, *99*, 739–755. [CrossRef]
34. Che, H.; Yang, L.; Liu, C.; Xia, X.; Wang, Y.; Wang, H.; Wang, H.; Lu, X.; Zhang, X. Long-term validation of MODIS C6 and C6. 1 Dark Target aerosol products over China using CARSNET and AERONET. *Chemosphere* **2019**, *236*, 124268. [CrossRef] [PubMed]
35. Rogozovsky, I.; Ansmann, A.; Althausen, D.; Heese, B.; Engelmann, R.; Hofer, J.; Baars, H.; Schechner, Y.; Lyapustin, A.; Chudnovsky, A. Impact of aerosol layering, complex aerosol mixing, and cloud coverage on high-resolution MAIAC aerosol optical depth measurements: Fusion of lidar, AERONET, satellite, and ground-based measurements. *Atmos. Environ.* **2021**, *247*, 118163. [CrossRef]
36. Almeida, S.M.; Pio, C.; Freitas, M.C.; Reis, M.; Trancoso, M.A. Approaching PM2.5 and PM2.5-10 source apportionment by mass balance analysis, principal component analysis and particle size distribution. *Sci. Total Environ.* **2006**, *368*, 663–674. [CrossRef] [PubMed]
37. Xing, Y.-F.; Xu, Y.-H.; Shi, M.-H.; Lian, Y.-X. The impact of PM2.5 on the human respiratory system. *J. Thorac. Dis.* **2016**, *8*, E69.
38. Zhang, F.; Shi, Y.; Fang, D.; Ma, G.; Nie, C.; Krafft, T.; He, L.; Wang, Y. Monitoring history and change trends of ambient air quality in China during the past four decades. *J. Environ. Manag.* **2020**, *260*, 110031. [CrossRef] [PubMed]
39. Goldberg, D.L.; Gupta, P.; Wang, K.; Jena, C.; Zhang, Y.; Lu, Z.; Streets, D.G. Using gap-filled MAIAC AOD and WRF-Chem to estimate daily PM2.5 concentrations at 1 km resolution in the Eastern United States. *Atmos. Environ.* **2019**, *199*, 443–452. [CrossRef]

40. Wang, X.; Sun, W. Meteorological parameters and gaseous pollutant concentrations as predictors of daily continuous PM2.5 concentrations using deep neural network in Beijing–Tianjin–Hebei, China. *Atmos. Environ.* **2019**, *211*, 128–137. [CrossRef]
41. Li, Y.; Shi, G.; Sun, Z. Evaluation and improvement of MODIS aerosol optical depth products over China. *Atmos. Environ.* **2020**, *223*, 117251. [CrossRef]
42. Pu, Q.; Yoo, E.-H. Ground PM2.5 prediction using imputed MAIAC AOD with uncertainty quantification. *Environ. Pollut.* **2021**, *274*, 116574. [CrossRef] [PubMed]
43. Fu, D.; Song, Z.; Zhang, X.; Xia, X.; Wang, J.; Che, H.; Wu, H.; Tang, X.; Zhang, J.; Duan, M. Mitigating MODIS AOD non-random sampling error on surface PM2.5 estimates by a combined use of Bayesian Maximum Entropy method and linear mixed-effects model. *Atmos. Pollut. Res.* **2020**, *11*, 482–490. [CrossRef]
44. Lee, S.; Park, S.; Lee, M.I.; Kim, G.; Im, J.; Song, C.K. Air Quality Forecasts Improved by Combining Data Assimilation and Machine Learning With Satellite AOD. *Geophys. Res. Lett.* **2022**, *49*, e2021GL096066. [CrossRef]
45. He, Q.; Li, C.; Geng, F.; Yang, H.; Li, P.; Li, T.; Liu, D.; Pei, Z. Aerosol optical properties retrieved from Sun photometer measurements over Shanghai, China. *J. Geophys. Res. Atmos.* **2012**, *117*, D16204. [CrossRef]
46. Hsu, N.C.; Herman, J.; Torres, O.; Holben, B.; Tanre, D.; Eck, T.; Smirnov, A.; Chatenet, B.; Lavenu, F. Comparisons of the TOMS aerosol index with Sun-photometer aerosol optical thickness: Results and applications. *J. Geophys. Res. Atmos.* **1999**, *104*, 6269–6279. [CrossRef]
47. Che, H.; Qi, B.; Zhao, H.; Xia, X.; Zhang, X. Aerosol optical properties and direct radiative forcing based on measurements from the China Aerosol Remote Sensing Network (CARSNET) in eastern China. *Atmos. Chem. Phys.* **2018**, *18*, 405–425. [CrossRef]
48. Che, H.; Zhang, X.; Chen, H.; Damiri, B.; Goloub, P.; Li, Z.; Zhang, X.; Wei, Y.; Zhou, H.; Dong, F. Instrument calibration and aerosol optical depth validation of the China Aerosol Remote Sensing Network. *J. Geophys. Res. Atmos.* **2009**, *114*, D03206. [CrossRef]
49. Smirnov, Z.A.; Holben, B.N.; King, M.; Kaufmaq, Y.J.; Eck, T.F.; Slutsker, I. Accuracy assessments of aerosol optical properties retrieved from aerosol robotic network (aeronet) sun and sky radiance measurments. *J. Geophys. Res. Atmos.* **2013**, *105*, 9791–9806.
50. Smirnov, A.; Holben, B.N.; Eck, T.F.; Dubovik, O.; Slutsker, I. Cloud-Screening and Quality Control Algorithms for the AERONET Database. *Remote Sens. Environ.* **2000**, *73*, 337–349. [CrossRef]
51. Bessho, K.; Date, K.; Hayashi, M.; Ikeda, A.; Imai, T.; Inoue, H.; Kumagai, Y.; Miyakawa, T.; Murata, H.; Ohno, T. An introduction to Himawari-8/9—Japan's new-generation geostationary meteorological satellites. *J. Meteorol. Soc. Jpn. Ser. II* **2016**, *94*, 151–183. [CrossRef]
52. Japan Meteorological Agency. *Himawari–8/9 Himawari Standard Data User's Guide (Version 1.3)*; Japan Meteorological Agency: Tokyo, Japan, 2017.
53. Jiang, T.; Chen, B.; Chan, K.K.Y.; Xu, B. Himawari-8/AHI and MODIS aerosol optical depths in China: Evaluation and comparison. *Remote Sens.* **2019**, *11*, 1011. [CrossRef]
54. Zhang, W.; Xu, H.; Zhang, L. Assessment of Himawari-8 AHI aerosol optical depth over land. *Remote Sens.* **2019**, *11*, 1108. [CrossRef]
55. Gao, L.; Chen, L.; Li, C.; Li, J.; Che, H.; Zhang, Y. Evaluation and possible uncertainty source analysis of JAXA Himawari-8 aerosol optical depth product over China. *Atmos. Res.* **2021**, *248*, 105248. [CrossRef]
56. Ishida, H.; Nakajima, T.Y. Development of an unbiased cloud detection algorithm for a spaceborne multispectral imager. *J. Geophys. Res. Atmos.* **2009**, *114*, D07206. [CrossRef]
57. Yoshida, M.; Kikuchi, M.; Nagao, T.M.; Murakami, H.; Nomaki, T.; Higurashi, A. Common retrieval of aerosol properties for imaging satellite sensors. *J. Meteorol. Soc. Jpn. Ser. II* **2018**, *96B*, 193–209. [CrossRef]
58. Kikuchi, M.; Murakami, H.; Suzuki, K.; Nagao, T.M.; Higurashi, A. Improved hourly estimates of aerosol optical thickness using spatiotemporal variability derived from Himawari-8 geostationary satellite. *IEEE Trans. Geosci. Remote Sens.* **2018**, *56*, 3442–3455. [CrossRef]
59. Chu, D.A.; Kaufman, Y.; Zibordi, G.; Chern, J.; Mao, J.; Li, C.; Holben, B. Global monitoring of air pollution over land from the Earth Observing System-Terra Moderate Resolution Imaging Spectroradiometer (MODIS). *J. Geophys. Res. Atmos.* **2003**, *108*, 4661. [CrossRef]
60. Lyapustin, A.; Wang, Y.; Korkin, S.; Huang, D. MODIS collection 6 MAIAC algorithm. *Atmos. Meas. Tech.* **2018**, *11*, 5741–5765. [CrossRef]
61. Lyapustin, A.; Wang, Y. *MODIS Multi-Angle Implementation of Atmospheric Correction (MAIAC) Data User's Guide*; NASA: Greenbelt, MD, USA, 2018.
62. Uppala, S.M.; Kållberg, P.; Simmons, A.J.; Andrae, U.; Bechtold, V.D.C.; Fiorino, M.; Gibson, J.; Haseler, J.; Hernandez, A.; Kelly, G. The ERA-40 re-analysis. *Q. J. R. Meteorol. Soc. J. Atmos. Sci. Appl. Meteorol. Phys. Oceanogr.* **2005**, *131*, 2961–3012. [CrossRef]
63. Yang, X.; Zhao, C.; Luo, N.; Zhao, W.; Shi, W.; Yan, X. Evaluation and Comparison of Himawari-8 L2 V1. 0, V2. 1 and MODIS C6. 1 aerosol products over Asia and the oceania regions. *Atmos. Environ.* **2020**, *220*, 117068. [CrossRef]
64. Zhang, Z.; Wu, W.; Fan, M.; Tao, M.; Wei, J.; Jin, J.; Tan, Y.; Wang, Q. Validation of Himawari-8 aerosol optical depth retrievals over China. *Atmos. Environ.* **2019**, *199*, 32–44. [CrossRef]
65. She, L.; Zhang, H.; Wang, W.; Wang, Y.; Shi, Y. Evaluation of the multi-angle implementation of atmospheric correction (MAIAC) aerosol algorithm for Himawari-8 data. *Remote Sens.* **2019**, *11*, 2771. [CrossRef]

66. Sun, L.; Li, R.-B.; Tian, X.-P.; Wei, J. Analysis of the temporal and spatial variation of aerosols in the Beijing-Tianjin-Hebei region with a 1 km AOD product. *Aerosol Air Qual. Res.* **2017**, *17*, 923–935. [CrossRef]
67. Wang, L.; Cai, K.; Si, Y.; Yu, C.; Zheng, H.; Li, S. Evaluation of Himawari-8 version 2.0 aerosol products against AERONET ground-based measurements over central and northern China. *Atmos. Environ.* **2020**, *224*, 117357. [CrossRef]
68. Lyapustin, A.; Wang, Y.; Laszlo, I.; Kahn, R.; Korkin, S.; Remer, L.; Levy, R.; Reid, J. Multiangle implementation of atmospheric correction (MAIAC): 2. Aerosol algorithm. *J. Geophys. Res. Atmos.* **2011**, *116*, D03211. [CrossRef]
69. Su, X.; Wang, L.; Zhang, M.; Qin, W.; Bilal, M. A high-precision aerosol retrieval algorithm (HiPARA) for advanced himawari imager (AHI) data: Development and verification. *Remote Sens. Environ.* **2021**, *253*, 112221. [CrossRef]
70. Zhang, Z.; Wu, W.; Fan, M.; Wei, J.; Tan, Y.; Wang, Q. Evaluation of MAIAC aerosol retrievals over China. *Atmos. Environ.* **2019**, *202*, 8–16. [CrossRef]
71. Filonchyk, M.; Yan, H.; Zhang, Z.; Yang, S.; Li, W.; Li, Y. Combined use of satellite and surface observations to study aerosol optical depth in different regions of China. *Sci. Rep.* **2019**, *9*, 6174. [CrossRef]
72. Zhang, M.; Ma, Y.; Shi, Y.; Gong, W.; Chen, S.; Jin, S.; Wang, J. Controlling factors analysis for the Himawari-8 aerosol optical depth accuracy from the standpoint of size distribution, solar zenith angles and scattering angles. *Atmos. Environ.* **2020**, *233*, 117501. [CrossRef]
73. Fu, D.; Song, Z.; Zhang, X.; Wu, Y.; Duan, M.; Pu, W.; Ma, Z.; Quan, W.; Zhou, H.; Che, H. Similarities and Differences in the Temporal Variability of PM2.5 and AOD between Urban and Rural Stations in Beijing. *Remote Sens.* **2020**, *12*, 1193. [CrossRef]
74. Lennartson, E.M.; Wang, J.; Gu, J.; Castro Garcia, L.; Ge, C.; Gao, M.; Choi, M.; Saide, P.E.; Carmichael, G.R.; Kim, J. Diurnal variation of aerosol optical depth and PM 2.5 in South Korea: A synthesis from AERONET, satellite (GOCI), KORUS-AQ observation, and the WRF-Chem model. *Atmos. Chem. Phys.* **2018**, *18*, 15125–15144. [CrossRef]
75. Xu, J.; Han, F.; Li, M.; Zhang, Z.; Xiaohui, D.; Wei, P. On the opposite seasonality of MODIS AOD and surface PM2.5 over the Northern China plain. *Atmos. Environ.* **2019**, *215*, 116909. [CrossRef]
76. Qu, W.; Wang, J.; Zhang, X.; Sheng, L.; Wang, W. Opposite seasonality of the aerosol optical depth and the surface particulate matter concentration over the north China Plain. *Atmos. Environ.* **2016**, *127*, 90–99. [CrossRef]
77. Zhang, Z.; Wang, W.; Cheng, M.; Liu, S.; Xu, J.; He, Y.; Meng, F. The contribution of residential coal combustion to PM2.5 pollution over China's Beijing-Tianjin-Hebei region in winter. *Atmos. Environ.* **2017**, *159*, 147–161. [CrossRef]
78. He, Q.; Wang, M.; Yim, S.H.L. The spatiotemporal relationship between PM 2.5 and aerosol optical depth in China: Influencing factors and implications for satellite PM 2.5 estimations using MAIAC aerosol optical depth. *Atmos. Chem. Phys.* **2021**, *21*, 18375–18391. [CrossRef]
79. Wu, Y.; Zhu, J.; Che, H.; Xia, X.; Zhang, R. Column-integrated aerosol optical properties and direct radiative forcing based on sun photometer measurements at a semi-arid rural site in Northeast China. *Atmos. Res.* **2015**, *157*, 56–65. [CrossRef]
80. Lekinwala, N.L.; Bhardwaj, A.; Raman, R.S.; Bhushan, M.; Bali, K.; Dey, S. A framework for setting up a country-wide network of regional surface PM2.5 sampling sites utilising a satellite-derived proxy–The COALESCE project, India. *Atmos. Environ.* **2020**, *234*, 117544. [CrossRef]
81. Harrison, R.M.; Pio, C.A. Size-differentiated composition of inorganic atmospheric aerosols of both marine and polluted continental origin. *Atmos. Environ.* **1983**, *17*, 1733–1738. [CrossRef]
82. Ouimette, J.R.; Flagan, R.C. The extinction coefficient of multicomponent aerosols. *Atmos. Environ.* **1982**, *16*, 2405–2419. [CrossRef]
83. Tang, Y.; Han, S.; Yao, Q.; Cai, Z.; Qiu, Y.; Feng, J. Analysis of a Severe Regional Haze-fog-dust Episode over North China in Autumn by Using Multiple Observation Data. *Aerosol Air Qual. Res.* **2020**, *20*, 2211–2225. [CrossRef]
84. Ma, S.; Zhang, X.; Gao, C.; Tong, Q.; Xiu, A.; Zhao, H.; Zhang, S. Simulating performance of CHIMERE on a late autumnal dust storm over Northern China. *Sustainability* **2019**, *11*, 1074. [CrossRef]
85. Wang, Z.; Pan, X.; Uno, I.; Li, J.; Wang, Z.; Chen, X.; Fu, P.; Yang, T.; Kobayashi, H.; Shimizu, A. Significant impacts of heterogeneous reactions on the chemical composition and mixing state of dust particles: A case study during dust events over northern China. *Atmos. Environ.* **2017**, *159*, 83–91. [CrossRef]